Nanoscale

Accepted Manuscript

This article can be cited before page numbers have been issued, to do this please use: E. A. Anumol, A. Enyashin, N. M. Batra, P. M. F. J. Costa and L. D. Francis, *Nanoscale*, 2016, DOI: 10.1039/C6NR02710E.

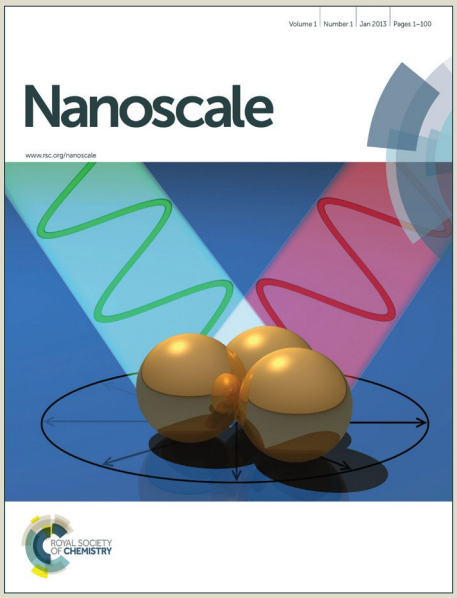

ROYAL SOCIETY OF CHEMISTRY

www.rsc.org/nanoscale

View Article Online
DOI: 10.1039/C6NR02710E

Structural and Chemical Analysis of Gadolinium Halides Encapsulated within WS_2 Nanotubes

E. A. Anumol,[a] Andrey N. Enyashin,[b] Nitin M. Batra,[c] Pedro M. F. J. Costa[c] and Francis Leonard Deepak [a,*]

The hollow cavities of nanotubes serve as templates for the growth of size- and shape-confined functional nanostructures, giving rise to novel materials and properties. In this work, considering their potential application as MRI contrast agents, gadolinium halides are encapsulated within the hollow cavities of WS_2 nanotubes by capillary filling to obtain $GdX_3@WS_2$ nanotubes (where X = Cl, Br or I and @ means encapsulated in). Aberration corrected scanning/transmission electron microscopy (S/TEM) and spectroscopy is employed to understand the morphology and composition of the $GdI_3@WS_2$ nanotubes. The three dimensional morphology is studied with STEM tomography but understanding the compositional information is non-trivial due to the presence of multiple high atomic number elements. Therefore, energy dispersive X-ray spectroscopy (EDS) tomography was employed revealing the three dimensional chemical composition. Molecular dynamics simulations of the filling procedure shed light into the mechanics behind the formation of the confined gadolinium halide crystals. The quasi-1D system employed here serves as an example of a TEM-based chemical nanotomography method that could be extended to other materials, including beam-sensitive soft materials.

[a] *International Iberian Nanotechnology Laboratory (INL), Avenida Mestre Jose Veiga, Braga 4715-330, Portugal, E-mail: leonard.francis@inl.int*
[b] *Ural Federal University, Institute of Mathematics and Computer Sciences, Turgeneva Str., 4, 620083 Ekaterinburg, Russian Federation*
[c] *King Abdullah University of Science and Technology, Physical Science and Engineering Division, Thuwal 23955-6900, Saudi Arabia*
† Electronic Supplementary Information (ESI) available: Additional figures and experimental data.

View Article Online
DOI: 10.1039/C6NR02710E

Introduction

Nanotubes including those of carbon, BN and WS_2 have been widely investigated for a variety of applications.[1, 2] The properties of these nanotubes depend on the number of layers, inner/outer diameters and aspect ratio. The synthesis of carbon and inorganic nanotubes in large quantities and with different aspect ratios, varying inner/outer diameters added to tailored electronic properties can now be feasibly directed towards specific applications.[2-4] In addition to the unique properties inherent to these one dimensional nanostructures, the presence of well-defined cavities makes nanotubes ideal unidirectional templates for the growth of confined substances resulting in hetero-structures with improved/novel properties.[5,6] The nanotube host can also help improving the long-term chemical stability of the encapsulated materials[7] or act as vehicle for delivery of minute quantities of guest substances.[8]

Capillary filling has been widely employed to encapsulate metals, metal halides and other compounds in CNTs.[6,9] In order to achieve this, the compounds are annealed above their melting point, along with the nanotubes, and are subsequently cooled. Capillary filling can be extended to the encapsulation of metals and metal halides in inorganic nanotubes such as WS_2, MoS_2, BN, etc. For example, 1D crystals of CsI were encapsulated in WS_2 nanotubes.[10] Additionally, layered compounds such as PbI_2, BiI_3, and SbI_3 were employed to obtain core-shell inorganic nanotubes.[11,12] Magnetically active Gd^{3+} composites are favorable for various biomedical applications. Gd^{3+}@ultra-short carbon nanotubes were shown as a high performance MRI contrast agent.[13] Encapsulation of GdI_3 in MWCNTs and their magnetic properties was reported recently where the encapsulated Gd compounds remained paramagnetic, positioning it as a potential MRI contrast agent.[14] It should also be noted here that cytotoxicity studies on WS_2 nanotubes reported its safety doses and potential for use in biomedical applications.[15]

Considering this intriguing aspect, in the present study we have carried out capillary filling of Gd-based compounds in WS_2 nanotubes. Thus GdX_3 (where X = Cl, Br, I) filled WS_2 nanotubes was obtained and subsequently characterized employing S/TEM and associated spectroscopic techniques which serve as ideal tools in determining structure and composition with high spatial resolution in the nano/sub-nanoscale, essential for its further applications.[16] The structure and morphology of the GdI_3@WS_2 nanotubes are investigated using HAADF-STEM. Though HAADF imaging has strong Z dependence, when there are multiple elements in the material with similar atomic numbers (as in the present case of GdI_3@WS_2), interpretation of chemical information from HAADF-STEM is not reliable. In these cases, nanoscale chemical analysis in three dimensions could be achieved using spectroscopic electron tomography methods. Thus three dimensional chemical mapping of the GdI_3@WS_2 nanotubes, is carried out using EDS tomography. To the best of our knowledge such a study with similar atomic number constituents (ex: GdI_3@WS_2 composite nanotube) is done for the first time employing EDS-Tomography in order to understand the structure and chemistry in three dimension at the nanoscale. In order to reduce the beam induced effects on the specimen,

View Article Online
DOI: 10.1039/C6NR02710E

tomography experiments are carried out at 80 kV and irradiation effects are investigated at different accelerating voltages, probe current and electron doses. Apart from GdI_3, the synthesis is also carried out employing both $GdBr_3$ and $GdCl_3$ for the filling of WS_2 nanotubes. In order to understand the difference in behavior of the different halides towards the filling of WS_2 nanotubes, Molecular Dynamics (MD) simulations are carried out. MD simulations of the capillary filling of the gadolinium halide melts in WS_2 nanotubes are performed to study the kinetics of imbibition and to compare the filling of the gadolinium halides (GdI_3 vs $GdBr_3$ vs $GdCl_3$) in WS_2 nanotubes. The results obtained from MD simulations agree very well with the observed experimental observations.

Experimental

Synthesis

The gadolinium halide filled WS_2 nanotubes were obtained by capillary filling. WS_2 nanotubes mixed with gadolinium iodide in the weight ratio of 1:5, 1:7 and 1:10 were sealed in quartz ampules under vacuum. The mixtures in sealed ampules were annealed at 1000 °C for 168 hours. Subsequent to the reaction the ampules were broken and the product was collected for further characterization. A similar method was employed for $GdBr_3$ and $GdCl_3$ filling of WS_2 NTs. The experimental conditions are tabulated in Supporting Information, Table S1-3.

Characterization

To prepare the specimen for TEM/STEM, the samples were dispersed in ethanol by ultrasonication and a drop of this dispersion was placed on a holey carbon grid and dried. TEM/STEM analysis at both 80 kV and 200 kV was performed on FEI Titan ChemiSTEM equipped with probe corrector, Super-X EDS detector and Gatan EELS spectrometer. EDS Quantification was carried out by employing the Cliff-Lorimer method in Esprit Software. Electron Energy Loss Spectroscopy (EELS) and Energy Filtered-TEM (EFTEM) were carried out using Gatan Digital Micrograph. The three window method was used for obtaining EFTEM elemental maps. EELS spectrum images were acquired using Tecnai Imaging and Analysis (TIA) software. AC-HRTEM imaging was carried out on Titan Themis TEM equipped with both probe Cs corrector and image Cs corrector, operated at 200 kV. Electron Tomography experiments were carried out at 80 kV. A convergence angle of 12 mrad and a probe current of 0.5 nA was used. For HAADF-STEM tomography, the specimen was loaded on a FEI single tilt holder. Automated tilt series acquisition was done using the tomography component in TIA software, in the tilt range of -57° to +70° using 2° steps up to 50° and 1° steps at higher angles. The tilt series was aligned and reconstructed in Inspect 3D using simultaneous iterative reconstruction technique (SIRT) algorithm and rendered in Amira software. For EDS tomography, a semi-automated acquisition was used to incorporate the EDS acquisition at each tilt angle. A higher tilt step of 3°/4° was used to reduce the exposure time. EDS

View Article Online
DOI: 10.1039/C6NR02710E

acquisition was done for 180 seconds/240 seconds with a probe current of ~ 0.5/1 nA. Signals from all the four detectors in the Super-X EDS system were collected and the Esprit software was used to acquire the elemental maps. The tilt series was aligned and reconstructed using Inspect 3D and rendered in Amira software in a method similar to that of HAADF-STEM tomography. Structure models were created with Crystal Maker software. The HRTEM and electron diffraction simulations were carried out using QSTEM[17] and SimulaTEM[18] employing similar microscope parameters to those used in the experimental work.

MD simulations

In our theoretical description of capillary filling we do not consider a steady-state capillary flow, but pay attention on the filling of nanotubes by a finite amount of matter as it can be realized in the experiments. The starting models for MD annealing and equilibration of molten halide drops were carved as the spheres from corresponding bulk crystals and each included 1000 GdX_3 stoichiometric units (4000 atoms). After equilibration their final structures were used as starting models for study of imbibition into a WS_2 nanotube. Model of WS_2 nanotube was based on cluster composed of 25 unit cells of double-walled *zigzag* (30,0)@(42,0) nanotube with 2H-WS_2 polytypic arrangement (diameters of 30.2 and 42.3 Å measured for coaxial W atomic cylinders, 10800 atoms in total). The apex of nanotube was installed initially at 5 Å from the edge of equilibrated drop. Further, WS_2 nanotube was considered as a rigid body. MD simulations of all nanostructures have been performed using in-house code as for canonical ensembles at temperature T = 1300 K. Temperature was controlled in all simulations with the velocity scaling. Newton's equations of motion were integrated with the time step of 5 fs via the Verlet leapfrog algorithm during 2 ns for annealing and at least 4.6 ns for imbibition simulations. The force-field level of theory was applied for these nanosecond simulations. Interactions within the GdX_3 melts and between the melts and WS_2 nanotube were described using Coulomb and Lennard-Jones potentials as parametrized in framework of Universal Force Field (UFF).[19] To estimate the atomic charges for GdX_3 and WS_2, the Pauling scheme using Pauling electronegativities was applied ($W^{+1.36}S_2^{-0.68}$, $Gd^{+2.58}Cl_3^{-0.86}$, $Gd^{+2.31}Br_3^{-0.77}$, $Gd^{+2.13}I_3^{-0.71}$). The truncation at 12 Å for all short-range non-bonded interactions was used, while the long-range electrostatic interactions were computed without any restriction and approximation. In addition, validating the force-field scheme chosen as for purely ionic compounds, the predominant ionic character of GdX_3 compounds and the absence of any Gd-Gd covalent bonding compounds were disclosed using DFT GGA calculations of $GdCl_3$ and GdI_3 crystals as implemented in SIESTA software (Fig. S13).[20] Visualization of atomic structure and MD trajectories was performed using VMD software (http://www.ks.uiuc.edu/Research/vmd/).[21]

Results and discussion

Characterization of GdI_3 filled within WS_2 nanotubes

View Article Online
DOI: 10.1039/C6NR02710E

The GdI_3@WS_2 nanotube obtained by capillary filling at 1000 °C, employing a weight ratio of 1:5 WS_2 to GdI_3 and a reaction time of 72 h (see Table S1 for experimental conditions of the filling experiments), is shown in Fig. 1. The TEM bright field image and HAADF-STEM images in Fig. 1a and 1b respectively, show that the hollow cavity of the nanotube is filled by crystalline rod-like structure. The bright contrast in Fig. 1b originates from the presence of GdI_3 filling within the WS_2 nanotube. A schematic representation of the capillary filling is shown in Scheme S1. EDS spectrum (Fig. 1c) confirms the presence of W, S, Gd and I; the signals of Gd and I originating from the filling within the WS_2 nanotube. The EDS quantification is shown in Table S4. The atomic percentage of Gd and I present in the sample corresponds to 1:3 ratio confirming the presence of GdI_3. The elemental maps of W, S, Gd and I, corresponding to the HAADF image in Fig. 1d, are shown in Fig. 1e-h, which clearly distinguishes between the WS_2 nanotube walls and the interior GdI_3 which is within the core of the WS_2 nanotube. Fig. S1 shows a WS_2 nanotube of a smaller inner diameter with Gd and I incorporated within the core of the NT. The GdI_3 filling in the hollow part of WS_2 clearly shows a continuous rod-like structure. Fig. S2 shows the HAADF image and the corresponding respective EDS maps showing a partial GdI_3 filling in a WS_2 nanotube. The WS_2 nanotube sample used in this study, consists mainly of open ended nanotubes with diameter > 40 nm. Based on the TEM images and compositional analysis with EDS, it is confirmed that about 60% of the nanotubes are filled with GdI_3.

EELS spectra were recorded to confirm the chemical composition and nature of the iodide phase in the composite nanotube. Fig. 2a shows the HAADF image of the GdI_3 filled WS_2 nanotube and their corresponding EELS spectrum is shown in Fig. 2b. The spectrum reveals the presence of the I $M_{4,5}$ edge at 625 eV and Gd $M_{4,5}$ edge at 1184 eV. There was no O K signal in the EELS spectrum as well as EDS spectrum (ref: Fig. 1c) showing that the GdI_3 is stable within the nanotube and no oxidation has occurred. The analysis also clearly revealed that there are no remnants of oxide from the synthesis of the nanotubes themselves.[10-12] The EELS signal at 1184 eV is characteristic of Gd^{3+}.[22] Previous studies have indicated that Gd^{3+} containing composites with CNT are magnetically active and therefore a potential MRI contrast agent.[14] Similarly in the present case the use of Gd@WS_2 NTs could find interesting applications related to medical imaging and diagnostics, a topic which needs to be explored further suitably. EFTEM elemental maps of the GdI_3@WS_2 NT are shown in Fig. 2c-e. The elemental maps are obtained by the three window method. The combined map with all the elements overlaid is shown in Fig. 2f. The presence of GdI_3 within the core of the WS_2 nanotube is thus clearly evident.

Characterization of surface coated GdI_3 on the WS_2 nanotubes

When the ratio of WS_2:GdI_3 was increased to 1:7, an increase in the efficiency of filling was observed. A further increase to 1:10 resulted in significant increase in the filling as well as coating of GdI_3 on the surface of the nanotube as shown in Fig. S3. TEM

View Article Online
DOI: 10.1039/C6NR02710E

image (Fig. S3a) and HAADF-STEM image (Fig. S3b) show the presence of GdI_3 on the surface of the nanotube, in addition to that of the filling, as indicated by the blue arrows. Low magnification HAADF image of a nanotube with flake-like surface growth of GdI_3 on WS_2 is shown in Fig. S3c along with the EELS spectrum images revealing that the flake-like features consists of Gd and I. The EELS spectrum obtained from the flake shows the characteristic I $M_{4,5}$ edge at 625 eV and the Gd $M_{4,5}$ edge at 1184 eV (Fig. S3d).[22]

Apart from GdI_3, experiments were also carried out under similar experimental conditions employing $GdBr_3$ and $GdCl_3$ (see Table 2 and Table 3 for experimental conditions of the filling experiments) to enable capillary filling in WS_2 nanotubes. In the case of $GdBr_3$, mainly surface coating of the WS_2 nanotubes was observed (Fig. S4) and the filling efficiency was considerably lower (< 5 %). In the case of $GdCl_3$, no filling was observed under similar experimental conditions.

Nanotube formation of GdI_3 in WS_2 nanotubes

In addition to the rod-like morphology of GdI_3 formed within the core of the WS_2 nanotubes, in some cases it is also possible to obtain a nanotube-like structure of GdI_3 forming within the WS_2 nanotubes (Fig. 3a). GdI_3 has a layered-like structure akin to carbon, BN or MoS_2/WS_2 and hence can form the nanotube structure. In the case of CNTs and WS_2 the inner diameter of the host nanotube controls the formation of the nanorod or nanotube, a larger diameter favoring the formation of nanotubes.[11,23] Cabana *et al.* observed a threshold diameter of 3.5 nm for the formation of PbI_2 nanotubes@CNTs.[23] In a study by Kreizman *et al*. on BiI_3 and PbI_2 filled WS_2 nanotubes, using experimental results and a theoretical model, a critical core diameter of 12 nm was obtained, above which the filling can result in core-shell nanotubes and below which nanowires results.[11] In the present study, it is observed that the filling of GdI_3 results in the formation of continuous rod-like structure within the WS_2 nanotube in most cases independent of the diameter of the nanotube, although nanotube-like morphology is observed in some cases. Shown in Fig. 3b-e, are the corresponding EELS spectra of the GdI_3-WS_2 nanotubes. The spectra reveals the characteristic W-$M_{4,5}$, S-$L_{2,3}$ edge, Gd-$M_{4,5}$ edge at 1184 eV and I-$M_{4,5}$ edge at 625 eV. The corresponding Gd-map extracted from the GdI_3 nanotube-like structure is shown in Fig. 3f.

Identification of the crystal structure and phase of GdI_3

Fig. 4a shows a representative AC-HRTEM micrograph of the GdI_3@WS_2 nanotube (obtained from the sample with WS_2:GdI_3 weight ratio of 1:7). The WS_2 nanotube consists of ~45 layers with an inner diameter of ~40 nm and outer diameter of ~95 nm. The interlayer spacing is 0.62 nm. The presence of the encapsulated rod-like GdI_3 crystal is clear, along with its termination as a convex meniscus. In Fig. 4b, a longitudinal-cut model of the composite nanotube is viewed, aligned with the structure in Fig. 4a.

View Article Online
DOI: 10.1039/C6NR02710E

For clarity, only the three innermost WS_2 tubes were included in the model. To illustrate the GdI_3 core, the structural parameters provided by the PDF Card No: 04-007-3286 were used. This idealized composite nanotube (or sections of it) was used to provide additional structural insight by HRTEM image simulation (Fig. S5-S7). The Fourier transform (FFT) analysis of the HRTEM micrograph in Fig. 4a was separated in two distinct regions, the empty (region I) and the filled nanotube (region II). Accordingly, the FFT in Fig. 4c shows a ring of reflections, typical of layered materials with rotational stacking faults. The frequency of the ring corresponds well with the $(0\bar{1}0)$ of the hexagonal WS_2 structure, space group $P6_3/mmc$. Analysis of the FFT elucidated that there are, at least, eight sets of reflections (Fig. 4d). This equates to the stacking of concentric nanotubes that are slightly rotated between each other and/or have different helicity. In region II, the FFT shows additional lower frequency reflections to those of the empty nanotube (Fig. 4e). To analyze the FFT, electron diffraction patterns were simulated for the encapsulated metal halide crystal (Fig. S8). As shown in Fig. 4f, the assignment indicates that the reflections are concurrent with the rhombohedral GdI_3 structure, space group $R\bar{3}$, oriented along the zone axis $<\bar{3}00>$. While other reflections were not entirely clear, both the spacing and angle for the 003 and 012 spots present an excellent match. The study of nanotube-confined 1D metal halide crystals is known to be challenging as lattice distortions such as contraction of interplanar distances as well as defects (plane shear),[24] and the onset of grains[25] take place in these composite structures. Overall, the structural analysis of the HRTEM micrographs agree with the EELS results, together providing conclusive evidence for the inclusion of GdI_3.

Electron tomography

Electron tomography is becoming increasingly important in the characterization of nanomaterials. In strongly diffracting crystalline materials, as the diffraction contrast in TEM changes drastically with tilt angles, TEM violates the projection requirement-a basic criterion of tomography reconstruction. Therefore HAADF-STEM tomography is employed where the contrast is a function of the thickness and atomic number of the elements present in the material.[26] When the constituent materials in a composite have a significant difference in atomic numbers then STEM tomography can give composition information in three dimensions. In the present study, HAADF-STEM tomography was carried out to reveal the three dimensional morphology of the GdI_3 filled WS_2 samples. Beam damage is a serious problem for tomography as the tilt series acquisition can take 1-2 hours and many of the materials of interest are beam sensitive. Considering this, an accelerating voltage of 80 kV was used to minimize the beam damage on the specimen during the tilt series acquisition. Tilt series was acquired on a nanotube aligned along the tilt axis. Fig. 5a shows volume rendered 3D visualization of a GdI_3@WS_2 nanotube sample where the filling was predominantly inside the nanotube (1:7 ratio). The brightness decreases from red to blue.

View Article Online
DOI: 10.1039/C6NR02710E

Tomography was done also on the sample where GdI_3 flakes were grown on the surface of WS_2 nanotube. The volume rendering is shown in Fig. 5b. From the tomogram it is seen that the GdI_3 nanosheets are wound around the surface of the WS_2 nanotube. Video1 (S16 Video-1) shows the 360° view of the tomogram. Thus the reconstruction of the tilt series and the volume rendering provides a three- dimensional visualization of the morphology of the GdI_3@WS_2 nanotubes.

EDS tomography

HAADF-STEM tomography could reveal the three dimensional morphology of GdI_3@WS_2 nanotubes, but identification of GdI_3 filling in WS_2 is non-trivial as the contrast in HAADF images depends on both mass and thickness. For instance, an effectively thinner region (the hollow part of the WS_2 nanotube) with a filling of a higher Z material like GdI_3 does not result in an increase in contrast with respect to the nanotube wall. A clear distinction is possible when there is a large difference in atomic number, for instance, GdI_3 in carbon nanotube or in a sample of uniform thickness, even when the difference in atomic number is small. EDS tomography could serve as a better tool to understand the chemical composition in three dimension as the chemical contrast is independent of such factors. The use of Super-X EDS detector in the present studies (incorporated in the Titan ChemiSTEM) with four SDD detectors around the specimen facilitates acquisition of EDS data during tilt series. Also the high collection efficiency of the detector enables the acquisition of reliable elemental maps in few minutes and therefore the EDS tilt series can be materialized.[27] A nanotube aligned parallel to the tilt axis was studied. The nanotube selected was in a region close to the center of the grid to minimize signal from the copper bar of the grid and to avoid the grid bar shadowing up to high tilt angles. The acquisition was carried out using a probe of 12 mrad convergence angle and 0.5 nA current. EDS acquisition was carried out for 3 minutes at every tilt. The experimental conditions lead to a total dose of ~ $2x10^5$ e/nm^2 during the tilt series acquisition. Fig. 6 shows the tomograms of the nanotube designating the HAADF intensity and the chemical composition in a GdI_3 filled WS_2 nanotube. Fig. 6a shows the vertical view of the nanotube. From left to right, HAADF-STEM tomogram, combined tomograms of each element and individual tomograms with elements color coded as blue (W), green (S), yellow (Gd) and red (I) are shown. W and S tomograms indicate the hollow cavity in the center of the nanotube, whereas Gd and I shows the continuous rod morphology located in the hollow cavity of W and S. Fig. 6b shows the corresponding cross-sectional view of the nanotube. The presence of Gd and I inside the WS_2 nanotube is undoubtedly evident from the tomograms. Video (S17 Video-2) shows the 360° visualization of the tomogram. A similar acquisition was carried out on the sample where GdI_3 was present predominantly on the surface of the WS_2 nanotubes. The tomograms are shown in Fig. S9. The chemical contrast is readily apparent from such a reconstruction.

View Article Online
DOI: 10.1039/C6NR02710E

Optimization of the EDS acquisition conditions is vital in such investigations as a significant probe current is required to obtain high signal to noise ratio in EDS, wherein an increase in probe current can cause beam damage of the specimen. A higher current of 1 nA and longer EDS exposure of 4 minutes was used for the acquisition of another tilt series to improve the EDS signal obtained. The electron dose during the experiment was ~ $5x10^5$ e/nm^2. The HAADF and EDS tomograms are shown in Fig. 7. The higher current and the longer exposure leading to a higher electron dose resulted in significant damage in the specimen, consequential in intermittent regions of Gd and I (S18-Video 3).

Effect of beam irradiation

In order to follow the beam induced transformation in the filled nanotubes, a thin-walled nanotube was chosen with an outer diameter of ~ 40 nm and inner diameter of ~ 20 nm. The nanotube was exposed to electron beam for various duration and HAADF-STEM images and EDS maps were recorded. Fig. 8 shows the nanotube exposed for different durations at 80 kV with a probe current 1.35 nA at the initial stage, after 40 minutes and after 60 minutes. The electron dose was 1.15 e/$Å^2$s. Considerable change in the filling was observed after 40 minutes of exposure. Rearrangement of I and Gd is explicitly visible. Further exposure up to 60 minutes shows that I is diffused throughout the nanorods. This could be due to the decomposition of GdI_3. EDS analysis shows that the iodine content decreased significantly at the end of the acquisition with respect to the initial stage indicating the loss of volatile iodine. A similar experiment at 80 kV using 0.64 nA probe current and a dose of 0.55 e/$Å^2$s did not show significant change in 30 minutes (Fig. S10). When the experiment was done at 200 kV considerable change in the filled nanotube was observed even at a lower current and electron dose (0.46 nA probe current and a dose of 0.40 e/$Å^2$s). (Fig. S11-12).

Molecular dynamics (MD) simulations

In order to better understand the results of experimental observations and puzzling difference in capillary activity of WS_2 nanotubes regarding the different Gd halide melts, molecular dynamics (MD) simulations at atomistic scale were carried out. Both the simulations of isolated molten drops of GdX_3 (X = Cl, Br, I) compounds, as well as their penetration into the hollow core of open-ended WS_2 nanotube, were performed. Despite the size limitation of the atomistic models accessible for MD simulations, the present study correctly reproduces the experimental observation of different behavior among molten Gd halides. Both inorganic and carbon narrow nanotubes like those employed for the present MD simulations should possess superior capillary activity weakly depending on their wettability, which can be detected already at the timescale of nanoseconds.[28, 29] However, the direct visualization of evolution of the model setup reveals an extremely low capillary action

View Article Online
DOI: 10.1039/C6NR02710E

between WS_2 nanotube and $GdCl_3$ or $GdBr_3$ melts (Fig. 9; S19-video 4 and S20-video 5). Despite of the attraction between these melts and the nanotube, the action halts after the instantaneous approach of drop to the open end of nanotube. The melts of both compounds adsorb along the circumference of the nanotube and the convex meniscus rising from the edge of the inner surface is formed. After that, during the entire MD simulation there is no formation of visible labile structures, which would steadily propagate along or separate from the main part of melt into deep region of the nanotubular cavity. The same WS_2 nanotube demonstrates rather stronger capillary activity for the case of GdI_3 melt (Fig. 9; S21-video 6). After the formation of the meniscus of adsorbed drop the Gd and I ions begin to enter slowly into nanotubular cavity. Labile single-atom thick openwork fragments from the edge of meniscus can be observed. They propagate along the inner surface of nanotube, though they do not coalesce into a stable inner coating on the basal sulfur surface of the nanotube.

To characterize kinetics of imbibition, the time function of the melt uptake was calculated for every halide (Fig. 10). The shape of the functions for $GdCl_3$ and $GdBr_3$ melts proves the stacking of the drops near the end of nanotube. Nearly constant number of penetrated atoms <*N*> is preserved during all MD process and corresponds to the number of atoms forming meniscus. In contrast, the uptake function for GdI_3 is monotonically increasing and can be correlated with a linear function. Previous theoretical studies have validated applicability of the classical macroscopic Lucas-Washburn equation for the description of imbibition of molten KI and PbI_2 in MoS_2 nanotubes,[28] which establishes the dependence $< N > \sim \sqrt{t}$. Though, this dependence may fail at early times, when liquid is accelerated by the capillary forces, and inertial effects can lead to $< N > \sim t$ dependence for the meniscus rise.[30] Thus, recent result evidences a steady, yet, slow penetration of GdI_3 melt into nanotubular cavity. Such behavior may manifest a specific internal structure of a liquid, e.g. chain-like shape of molecules or clustering (*vide infra*).

While the imbibition kinetics of GdI_3 into sulfide nanotube is different to that of formerly studied PbI_2,[28] the analysis of the radial distribution functions for Gd and I atoms within the nanotube shows that the melt in the confined space demonstrates a shell-like structure similar to PbI_2 (Fig. S14). Distinct alternation in Gd and I distribution is observed, where the first positively charged Gd shell is exposed to negatively charged sulfur surface of WS_2. Such interplay between counter-ions favors a more rapid surface diffusion of Gd ions. It could hint at their dominant role during imbibition as well as it could influence on composition of final (embedded) product. Indeed, the stoichiometry of GdI_3 melt entered into our narrow model nanotube was nearly $GdI_{2.7}$ (Fig. S14), which suggests some possible Iodine deficiency of GdI_3 encapsulated into inorganic nanotubes. In order to better understand the results of these MD simulations and explain the failed imbibition of $GdCl_3$ and $GdBr_3$ melts as well as a slow imbibition of GdI_3 melt into WS_2 nanotube the data of MD simulations of isolated drops of molten salts were analyzed. The analysis of pair distribution functions $g_{ij}(r)$ for Gd-Gd, Gd-X and X-X shows that all melts are in

View Article Online
DOI: 10.1039/C6NR02710E

amorphous liquid-like state (Fig. S14). However, their smoothed profiles possess multiple distinct peaks up to the distances 11-12 Å, reflecting the presence of an intermediate-range order.

Choosing the nearest-neighbor Gd-Gd interatomic distance ("pair") with the largest repulsive interaction as the reference, the internal structure of all melts can be clearly disclosed and the striking difference between the compounds can be realized (Fig. 10). The structures of $GdCl_3$ and $GdBr_3$ melts demonstrate a very heavy clustering and are represented by uniform frameworks with an ordering spanning beyond single Gd-Gd pair. Many chain-like structures, square-like and triangular cycles are visible in $GdCl_3$ and, in less degree, in $GdBr_3$ melts. Single halide-anions serve there as bridging atoms between Gd cations and/or migrate within such frameworks. Then, the structure of GdI_3 melt may be regarded as the opposite case, since the majority of clusters seems to be presented only by "isolated" Gd pairs and V-shaped Gd triplets.

A more relevant view at the clustering degree of the melts can be done using the histogram of distance-angle distribution between Gd-Gd pairs (Fig. 10). In the absence of any couple of such pairs at short distances or in the case of total disorder in their mutual orientation the distribution function is equal to zero. However, all three histograms for GdX_3 melts demonstrate the presence of non-zero regions, corresponding to some preferable orientations of Gd-Gd pairs. Again a close similarity between $GdCl_3$ and $GdBr_3$ and both in contrast to GdI_3 is remarkable. The narrow band between 2-3 Å corresponds to the presence of V-shaped Gd triplets and distorted tetrahedra and in all three compounds it has minimum near 50-55˚, i.e. the configuration close to equilateral triangle. The wide band between 3-4 Å corresponds to L-shaped Gd triplets, which partially form square-like cycles and distorted prisms or cubes. The band at 5 Å corresponds to nearly parallel alignment of two Gd-Gd pairs, i.e. square-like cycles. The region from 6 Å and above can be correlated with the couples of Gd-Gd pairs forming already three-dimensional solids and framework. Noticeably, these histograms prove a framework structure as the attribute of $GdCl_3$ and $GdBr_3$ melts, while GdI_3 melt demonstrates only a faint resemblance. In this manner, our study uncovers the framework structure of molten $GdCl_3$ at atomistic level, which was surmised in the past using Raman spectroscopy of pure melt and mixtures $GdCl_3$-KCl.[31]

The framework structure of a melt has important aftermath. The ions bound into and within framework should have dramatically low diffusion rate comparing to that of free moving ions. The self-diffusion constants D of ions within GdX_3 melts have been estimated from our MD data of the mean-square ion displacements and using Einstein's formula: $D(Gd_{GdCl3}) = 0.15 \cdot 10^{-6}$ cm^2/s, $D(Gd_{GdBr3}) = 0.64 \cdot 10^{-6}$ cm^2/s, $D(Gd_{GdI3}) = 7.92 \cdot 10^{-6}$ cm^2/s, D(Cl) $= 0.62 \cdot 10^{-6}$ cm^2/s, D(Br) $= 2.42 \cdot 10^{-6}$ cm^2/s, D(I) $= 12.83 \cdot 10^{-6}$ cm^2/s. The comparison between diffusion constants of cation and anion in the same compound reveals a higher mobility of anions. It agrees well with the exceeding number of anions and with the presence of two types: either constituting

View Article Online
DOI: 10.1039/C6NR02710E

the framework together with cations or migrating within the framework. Also, cations are mainly the constituents of the framework.

Remarkably, self-diffusion constant of Gd in molten GdI_3 is in one order of magnitude larger, than in other molten halides with pronounced framework structure. This result implicitly approves the peculiar virtue of GdI_3 as the most appropriate agent among considered halides for Gd encapsulation into nanotubes. However, the estimated mobility of Gd in molten GdI_3 also belongs to the state of cations still constrained within small clusters (pairs and triplets of Gd ions bridged by I ions) as our MD simulations reveal. Therefore, the penetration of GdI_3 along the nanotubular cavity is hindered due to the larger effective diameter of diffusing particles, than those for simple cations.

The results of our MD simulations suggest a few possible routes to increase capillary activity. First, an increase of the temperature could destruct the framework or the clusters within GdX_3 melts. However, the temperature employed in the experiment for $GdCl_3$ and $GdBr_3$ compounds is higher, than their melting points, and is already at the limit of their thermal stability. A further temperature increase might lead to evaporation of volatile halogens and to formation of reduced halides with strong metal-metal bonding.[32] Second, we have considered possible flow imbibition in the case of the drop diameters larger, than the inner diameter of nanotube. One could surmise a different injection mechanism by means of simple mechanistic entering of a drop with the diameter smaller, than the inner diameter of nanotube. Yet, our MD simulations at the first glance do not support such option for $GdCl_3$ (S22-video 7). Gd cations - the drivers of diffusion along inner sulfur surface – are strongly bounded into framework and surrounded by the cloud of Cl anions. The surface of a $GdCl_3$ drop possesses always a negative charge. The latter causes the repulsive interaction with inner sulfur surface (also negatively charged), which cannot be beaten by capillary forces. The small drop adsorbs and remains at the edge of WS_2 nanotube. Thus, apart from framework-like structure, the interplay between surface charges hinders even simple mechanistic entering of small $GdCl_3$ drops with the sizes less than the inner diameter of WS_2 nanotube. Noteworthy, pure ionic model of the force-field applied for these MD simulations is quite optimistic, since any covalent bonding between $GdCl_3$ melt and the edge of WS_2 nanotube is excluded from consideration. However, if such bonding would take a place, then the imbibition will be even more hindered.

Thus, most likely, the imbibition of GdX_3 melts could be facilitated after the destruction of framework structure or clusters using additives of alkali metal halides, which would dilute highly charged Gd ions. The preliminary hints at this route have been already given in the past.[31]

View Article Online
DOI: 10.1039/C6NR02710E

Conclusions

GdI_3@WS_2 nanotubes were synthesized by capillary filling. Aberration corrected electron microscopy and spectroscopy confirmed the presence of rhombohedral GdI_3 with the paramagnetic valence state of Gd, in the confined environment within the WS_2 nanotube. HAADF-STEM tomography reveals the three dimensional morphology of the GdI_3@WS_2 nanotubes whereas EDS-tomography revealed clearly the composition in three dimensions of the GdI_3@WS_2 nanotube. The importance of optimization of microscope conditions and EDS acquisition for successful EDS tomography was demonstrated with the support of additional irradiation studies. This study demonstrates the successful use of EDS tomography to obtain nanoscale chemical composition of a multi-element core-shell structure, in three dimension unambiguously, which could now be extended to various other systems to follow phase transitions, alloying and sintering of nanocatalysts. The MD simulations in this work presents the first study of the capillary activity of inorganic WS_2 nanotubes in relation to the ionic melts with highly charged (trivalent) cations. MD simulations showed that the non-uniform behavior of the gadolinium halides towards capillary filling in WS_2 is due to the formation of a framework structure within $GdCl_3$ and $GdBr_3$ ionic melts unlike that of GdI_3, which dramatically decreases the self-diffusion constants of ions and strictly prohibits any mass transfer into the hollow core of WS_2 nanotubes.

Acknowledgements

The authors would like to thank Prof. Reshef Tenne (WIS) and Dr. Alla Zak (HIT) for providing the WS_2 nanotubes. The authors thank Dr. Manuel Banobre-Lopez for help with the filling of the ampoules. FLD and EAA acknowledge the financial support provided by the ERDF (ON.2 - O Novo Norte Program). ANE acknowledges the support by Act 211 Government of the Russian Federation, contract №. 02.A03.21.0006. NMB and PMFJC acknowledge funding from KAUST.

References

1 R. Tenne, *Front Phys* 2014, **9**, 370, R. Tenne, *Nature Nanotech.* 2006, **1**, 103.

2 D. Golberg, Y. Bando, C. C. Tang and C. Y. Zhi, *Adv. Mater.* 2007, **19**, 2413.

3 T. W. Ebbesen and P. M. Ajayan, *Nature* 1992, **358**, 220; S. Yasuda, A. Furuya, Y. Uchibori, J. Kim and K. Murakoshi, *Adv. Func. Mater.* 2016, **26**, 738.

4 N. G. Chopra, R. J. Luyken, K. Cherrey, V. H. Crespi, M. L. Cohen, S. G. Louie and A. Zettl, *Science* 1995, **269**, 966; A. Loiseau, F. Willaime, N. Demoncy, G. Hug and H. Pascard, *Phys. Rev. Lett.* 1996, **76**, 4737.

View Article Online
DOI: 10.1039/C6NR02710E

5 A. Ilie, J. S. Bendall, K. Nagaoka, S. Egger, T. Nakayama and S. Crampin, *ACS Nano* 2011, **5**, 2559; R. Kitaura, R. Nakanishi, T. Saito, H. Yoshikawa, K. Awaga and H. Shinohara, *Angew. Chem. Int. Ed.* 2009, **48**, 8298; T. Fujimori, A. Morelos-Gómez, Z. Zhu, H. Muramatsu, R. Futamura, K. Urita, M. Terrones, T. Hayashi, M. Endo, S. Young Hong, Y. Chul Choi, D. Tománek and K. Kaneko, *Nat Commun* 2013, **4**, 2162; C. E. Giusca, V. Stolojan, J. Sloan, F. Börrnert, H. Shiozawa, K. Sader, M. H. Rümmeli, B. Büchner and S. R. P. Silva, *Nano Lett.* 2013, **13**, 4020.

6 C. H. Kiang, J. S. Choi, T. T. Tran and A. D. Bacher, *J. Phys. Chem. C* 1999, **103**, 7449.

7 P. M. F. J. Costa, U. K. Gautam, Y. Bando and D. Golberg, *Carbon* 2011, **49**, 342.

8 P. M. F. J. Costa, U. K. Gautam, Y. Bando and D. Golberg, *Nat. Commun.* 2011, **2**, 421; P. M. F. J. Costa, U. K. Gautam, Y. Bando and D. Golberg, *Carbon* 2011, **49**, 3747.

9 E. Dujardin, T. W. Ebbesen, H. Hiura and K. Tanigaki, *Science* 1994, **265**, 1850; J. Sloan, D. M. Wright, S. Bailey, G. Brown, A. P. E. York, K. S. Coleman, M. L. H. Green, J. L. Hutchison and H.-G. Woo, *Chem. Comm.* 1999, *699*.

10 S. Hong, R. Popovitz-Biro, G. Tobias, B. Ballesteros, B. Davis, M. L. H. Green and R. Tenne, *Nano Res.* 2010, **3**, 170.

11 R. Kreizman, A. N. Enyashin, F. L. Deepak, A. Albu-Yaron, R. Popovitz-Biro, G. Seifert and R. Tenne, *Adv. Func.Mater.* 2010, **20**, 2459.

12 R. Kreizman, S. Y. Hong, J. Sloan, R. Popovitz-Biro, A. Albu-Yaron, G. Tobias, B. Ballesteros, B. G. Davis M. L. H. Green and R. Tenne, *Angew. Chem. Int. Ed.* 2009, **48**, 1230.

13 B. Sitharaman, K. R. Kissell, K. B. Hartman, L. A. Tran, A. Baikalov, I. Rusakova, Y. Sun, H. A. Khant, S. J. Ludtke, W. Chiu, S. Laus, E. Toth, L. Helm, A. E. Merbach and L. J. Wilson, *Chem. Comm.* 2005, 3915.

14 E. Fidiani, P. M. F. J. Costa, A. U. B. Wolter, D. Maier, B. Buechner, S. Hampel, *J. Phys. Chem. C* 2013, **117**, 16725.

15 J. T. Rashkow, Y. Talukdar, G. Lalwani and B. Sitharaman, *Nanomedicine* 2015, **10**, 1693.

16 F. L. Deepak, A. Mayoral, R. E. and Arenal (Eds.), *Advanced Transmission Electron Microscopy: Applications to Nanomaterials*, Springer 2015.

17 C. T. Koch, *Determination of core structure periodicity and point defect density along dislocations*, PhD Thesis, Arizona State University, 2002.

18 A. Gómez-Rodríguez, L. M. Beltrán-del-Río and R. Herrera-Becerra, *Ultramicroscopy* 2010, **110**, 95.

19 A. K. Rappe, C. J. Casewit, K. S. Colwell, W. A. Goddard and W. M. Skiff, *J. Am. Chem. Soc.* 1992, **114**, 10024.

20 J. M. Soler, E. Artacho, J. D. Gale, A. Garcia, J. Junquera, P. Ordejon, D. Sanchez-Portal, *J. Phys. Condens. Matter.* 2002, **14**, 2745.

21 W. Humphrey, A. Dalke and K. Schulten, *J. Mol. Graphics* 1996, **14**, 33.

View Article Online
DOI: 10.1039/C6NR02710E

22 K. Suenaga, S. Iijima, H. Kato and H. Shinohara, *Phys. Rev. B* 2000, **62**, 1627.

23 L. Cabana, B. Ballesteros, E. Batista, C. Magén, R. Arenal, J. Oró-Solé, R. Rurali, G. Tobias, *Adv. Mater.* 2014, **26**, 2016.

24 P. M. F. J. Costa, S. Friedrichs, J. Sloan and M. L. H. Green, *Chem. Mater.* 2005, **17**, 3122.

25 P. M. F. J. Costa, D. Golberg, M. Mitome, S. Hampel, A. Leonhardt, B. Buchner and Y. Bando, *Nano Lett.* 2008, **8**, 3120.

26 S. J. Pennycook, L. A. Boatner, *Nature* 1998, **336**, 565.

27 Pierre Burdet, Z. Saghi, A.N. Filippin, A. Borrás and P.A. Midgley, *Ultramicroscopy* 2016, **160**, 118; B. Goris, L. Polavarapu, S. Bals, G. Van Tendeloo, and L. M. Liz-Marzán, *Nano Lett.* 2014, **14**, 3220.

28 A. N. Enyashin, R. Kreizman and G. Seifert, *J. Phys. Chem. C* 2009, **113**, 13664.

29 A. N. Enyashin and G. Seifert, *Chem. Phys. Lett*. 2010, **501**, 98; C. Yang, X. Zhu, X. Lu and X. Feng, *J. Mol. Struc.(Theochem*) 2009, **896**, 6.

30 S. Supple and N. Quirke, , *J.Chem. Phys.* 2005, **122**, 104706.

31 A. Chrissanthopoulos and G. N. Papatheodorou, Phys. Chem. Chem. Phys. 2000, **2**, 3709; I. D. Zakir'yanova and A. B. Salyulev, *Russian Metallurgy (Metally)* 2010, **2**, 112.

32 K. Berroth, H. J. Mattausch and A. Simon, Z. Naturforschung B 1980, **35**, 626.

View Article Online
DOI: 10.1039/C6NR02710E

Figures

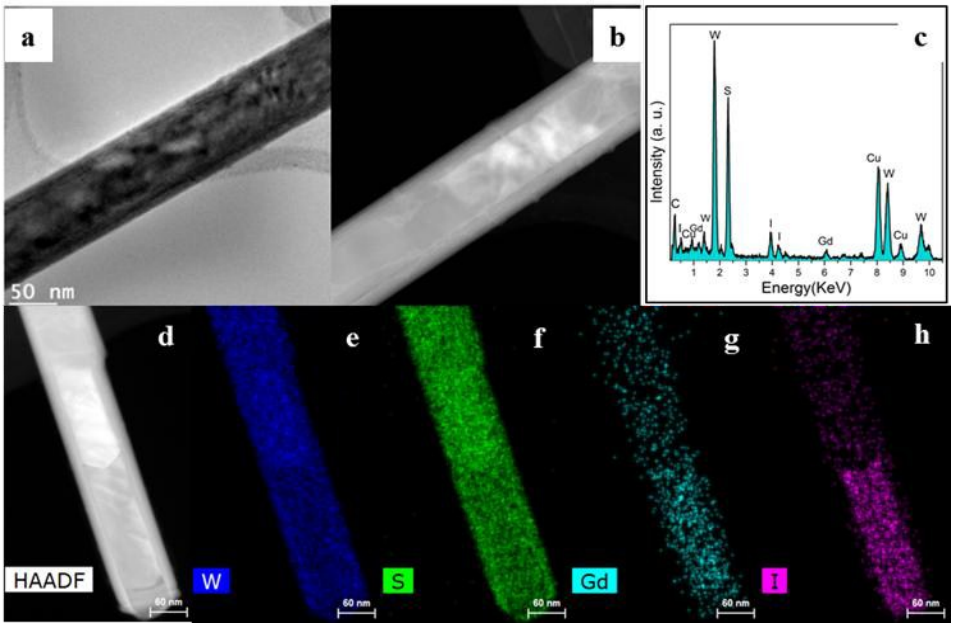

Fig. 1 a) and b) TEM bright field and HAADF-STEM images of the GdI_3 filled WS_2 nanotube, c) EDS spectrum, d) HAADF-STEM image and e-h) corresponding EDS elemental maps showing W Lα, S Kα, Gd Lα and I Lα signals of the GdI_3 filled WS_2 nanotubes, respectively.

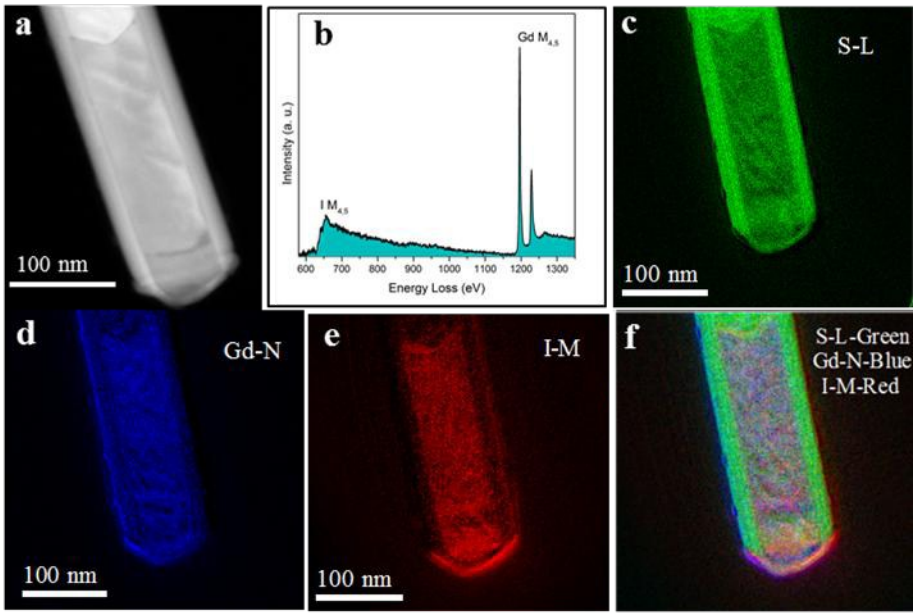

Fig. 2 a) HAADF-STEM image, b) EELS spectrum showing I $M_{4,5}$ and Gd $M_{4,5}$, c-f) EFTEM elemental maps, showing the presence of S-L (green), Gd-N (blue), I-M (red) and combined map with colors overlaid for the GdI_3 filled WS_2 nanotube.

View Article Online
DOI: 10.1039/C6NR02710E

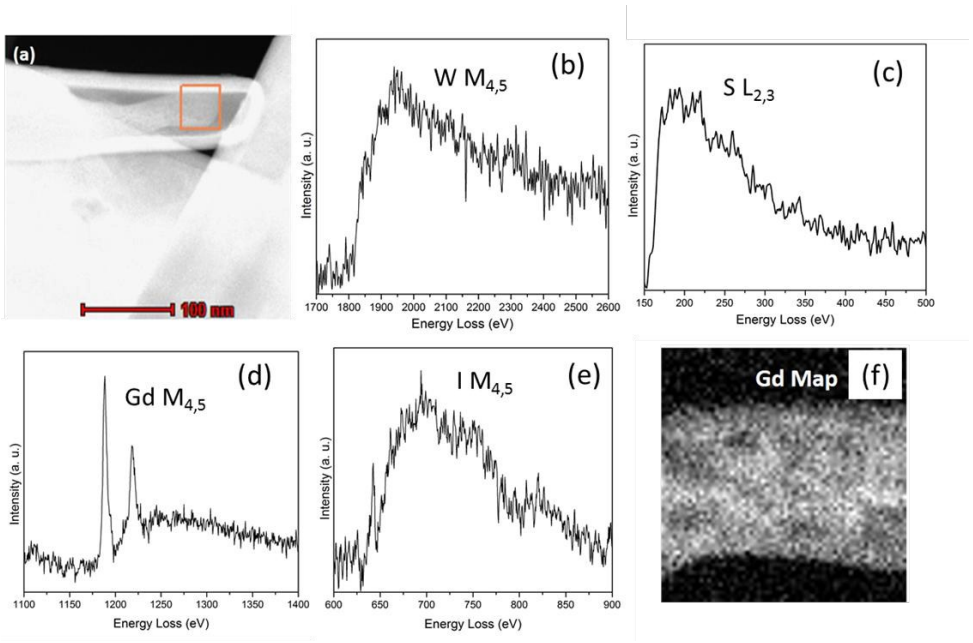

Fig. 3 a) HAADF-STEM image of hollow core-shell type GdI_3@WS_2 nanotube. b-e) are the EELS spectra showing W $M_{4,5}$, S $L_{2,3}$, Gd $M_{4,5}$ and I $M_{4,5}$ edges, respectively. f) Gd elemental map.

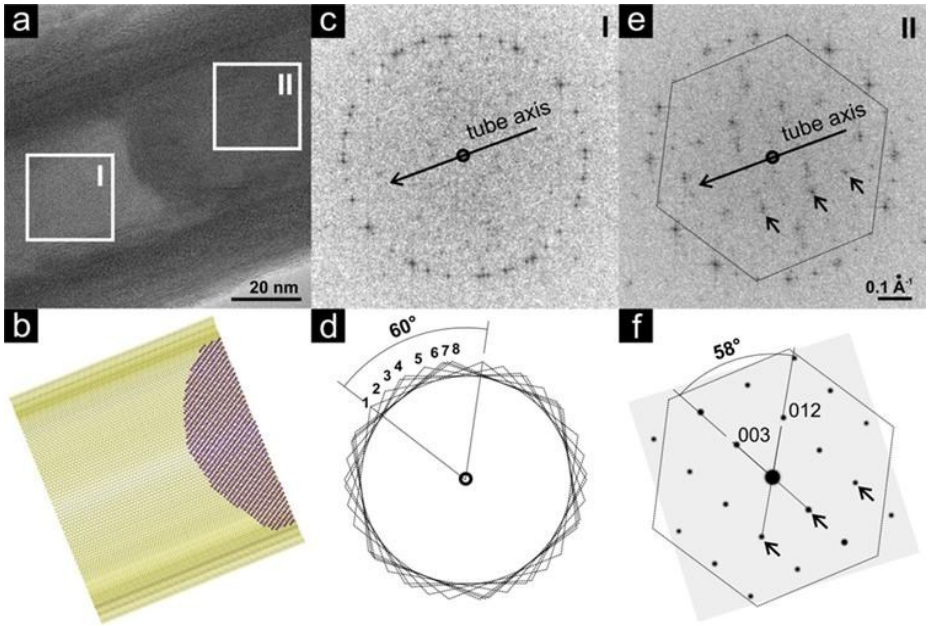

Fig. 4 a) AC-HRTEM image of GdI_3@WS_2 obtained using a 1:7 ratio; b) model of the structure in a), showing the empty and filled WS_2 sections along with the meniscus of the encapsulated GdI_3; c) FFT of section I, marked in a), where a ring of reflections at the same frequency is visible; d) the ring of reflections in c) can be decomposed into eight hexagons which is attributed to the stacking of at least eight concentric WS_2 tubes; e) FFT of section II, as marked in a), where besides the ring mentioned in c), additional reflections at lower frequency are seen and attributed to the encapsulated GdI_3 crystal (the hexagon marks one of the height sets of WS_2 reflections); f) simulated electron diffraction pattern of a $R\bar{3}$ GdI_3 crystal, along the low index zone axis $<\bar{3}00>$, where the assignment of the FFT in e) is made.

View Article Online
DOI: 10.1039/C6NR02710E

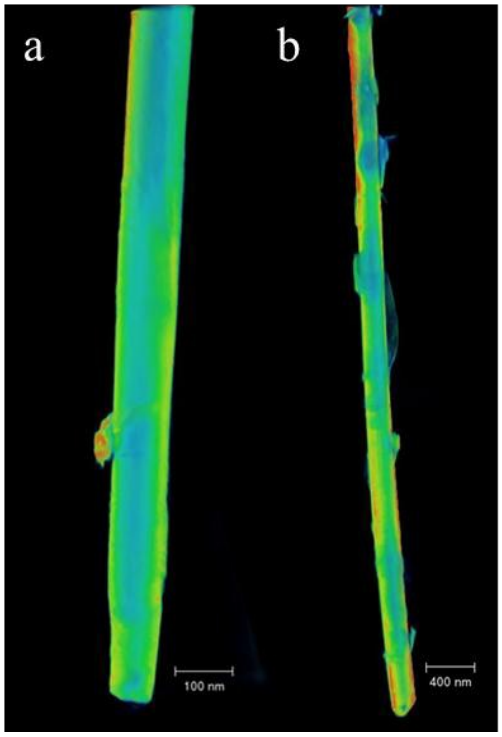

Fig. 5 Volume rendered 3D visualization of GdI_3@WS_2 nanotubes a) GdI_3 inside WS_2 b) GdI_3 on the surface of WS_2 nanotube

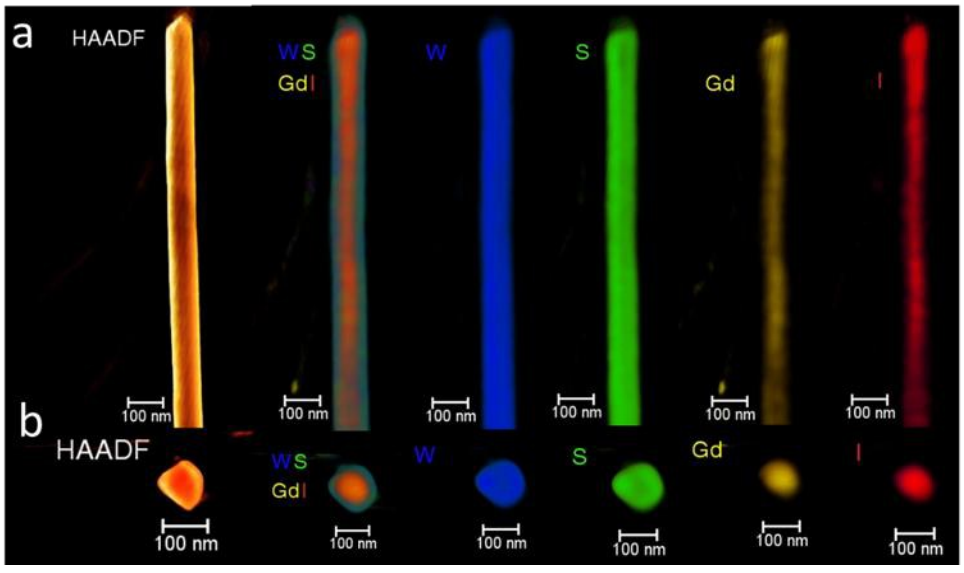

Fig. 6 Volume rendering of HAADF-STEM and EDS tomograms of GdI_3@WS_2 nanotube. a) Nanotube positioned vertically. From left to right, HAADF-STEM tomogram, combined tomograms of each element and individual elemental tomograms are given. b) Cross-sectional view of the nanotube. The elements are color coded as blue (W), green (S), yellow (Gd) and red (I).

View Article Online
DOI: 10.1039/C6NR02710E

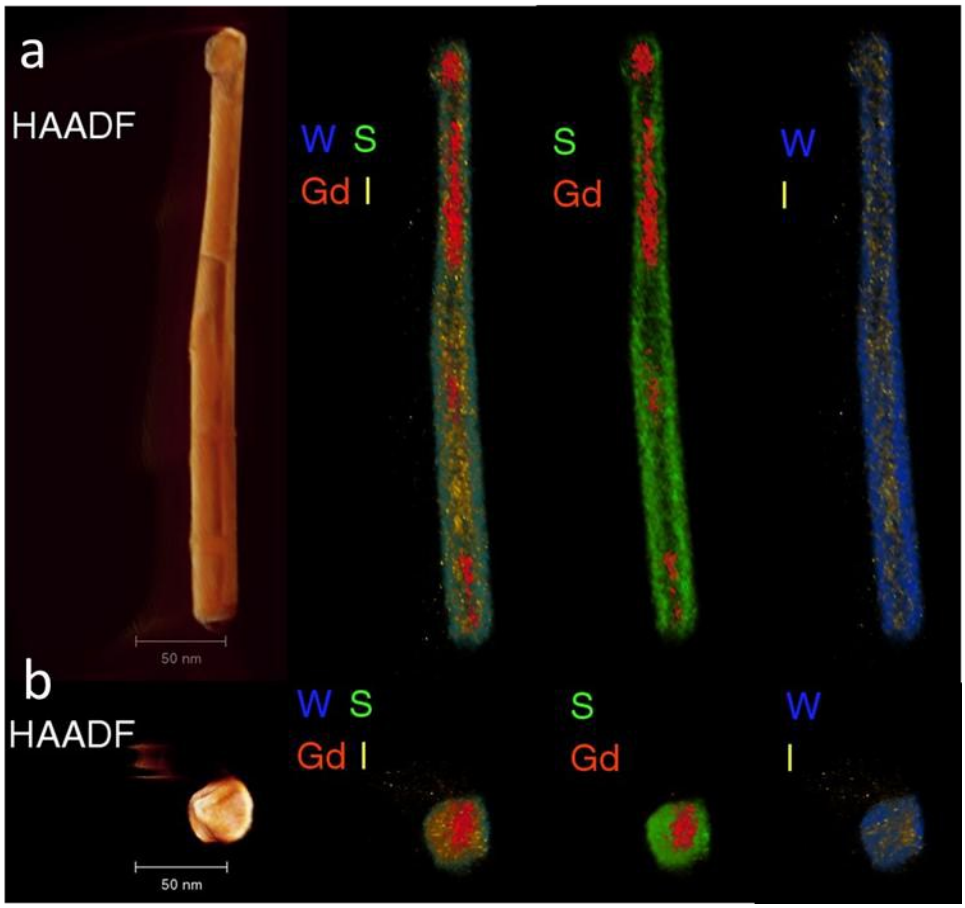

Fig. 7 Volume rendering of HAADF-STEM and EDS tomograms of GdI_3@WS_2 nanotube. a) A section of the nanotube positioned vertically and b) cross-sectional view of the nanotube. From left to right, HAADF-STEM, combined EDS tomograms of all elements, a combination of S and Gd and a combined tomogram of W and I are shown. In the color coding, blue is W, red is Gd, green is S and yellow is I.

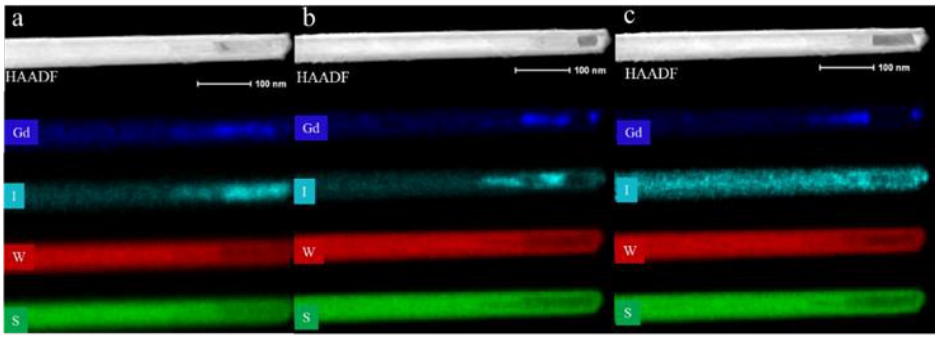

Fig. 8 HAADF-STEM and EDS elemental maps (Gd (blue), I (cyan), W (red), S (green)) of GdI_3 filled WS_2 a) at time 0, b) after 40 minutes and c) after 60 minutes. The experiment was done at 80 kV using 1.35 nA probe current and a dose of 1.15 e/$Å^2$s.

View Article Online
DOI: 10.1039/C6NR02710E

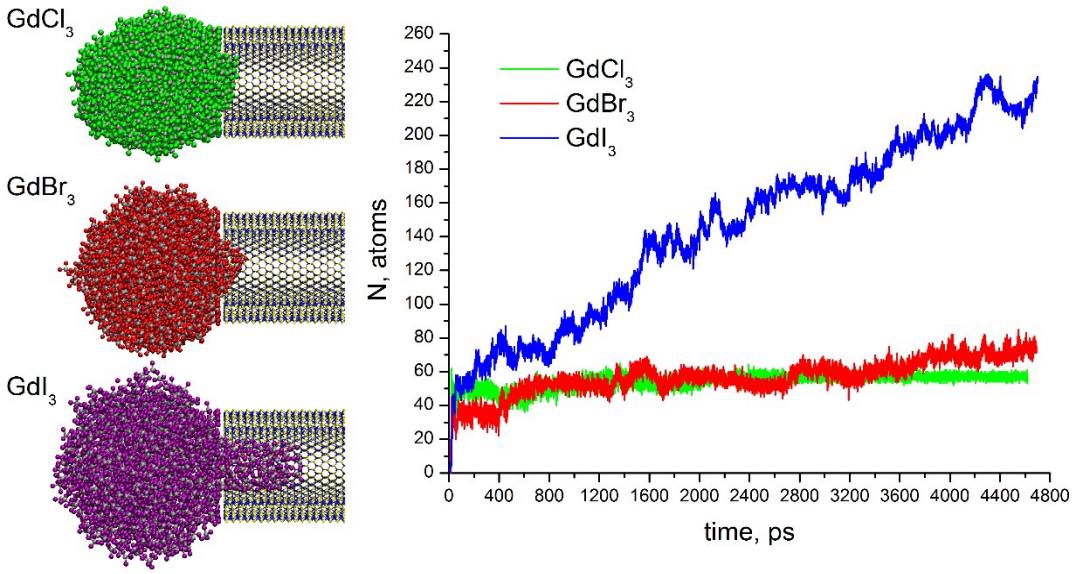

Fig. 9 Side views on the imbibition of GdX_3 drops (X = Cl, Br, I) in fragment of double-walled (30,0)@(42,0) 2H-WS_2 nanotube after MD simulations during 4.8 ns at T = 1300K. Frontal part of the nanotube wall is removed for clearness. Corresponding uptake (total number of atoms) as a function of time is depicted on the right panel.

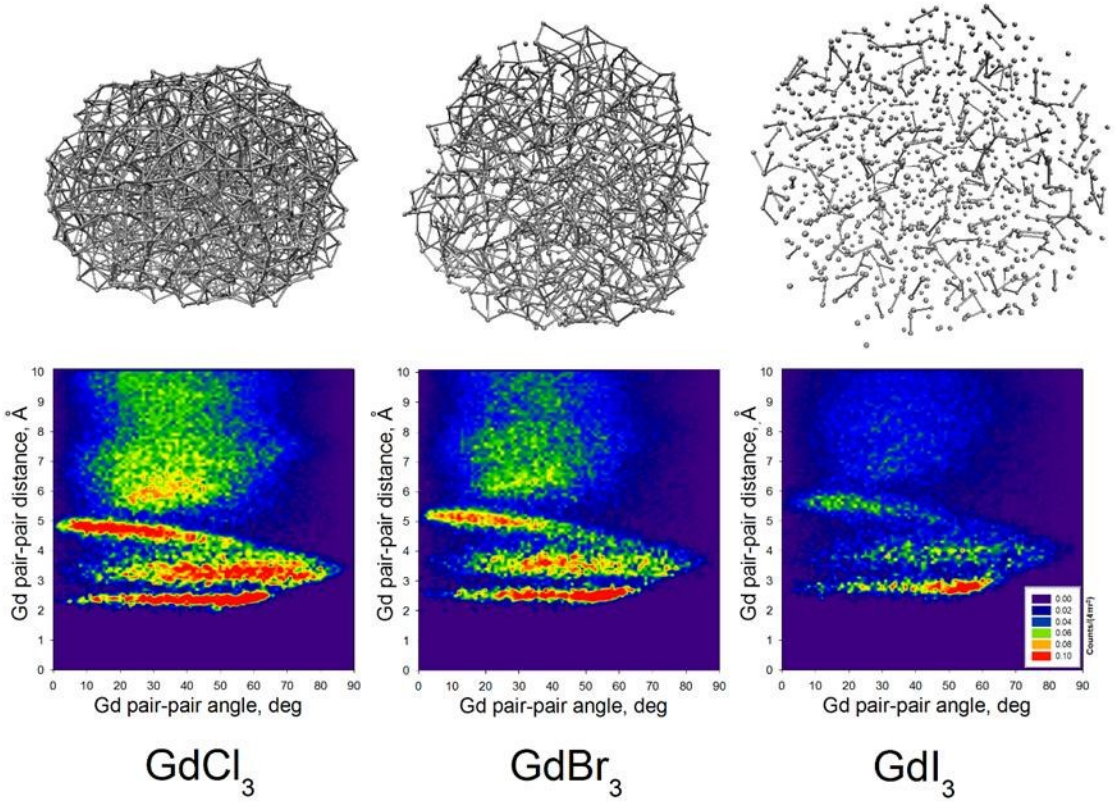

Fig. 10 Snapshots after MD annealing during 2 ns at T = 1300 K uncover the internal structure of GdX_3 drops (X = Cl, Br, I). Only Gd atoms and the nearest-neighbor Gd-Gd coupling ("Gd pair") are depicted for clearness (*on the top*). Heavy clustering is evident in the cases of $GdCl_3$ and $GdBr_3$. Identifying long-range order, the distance-angle distribution between Gd pairs is calculated and normalized by $1/(4\pi r^2)$ (*below*).